Electronic Supplementary Material (ESI) for Energy & Environmental Science.

Supporting Information for

Energetically Efficient Electrochemically Tunable Affinity Separation Using Multicomponent Polymeric Nanostructures for Water Treatment

Xianwen Mao, Wenda Tian, Yinying Ren, Dexin Chen, Sarah E. Curtis, Marjorie T. Buss, Gregory C. Rutledge, and T. Alan Hatton[*]

Department of Chemical Engineering, Massachusetts Institute of Technology, 77 Massachusetts Avenue, Cambridge, Massachusetts 02139, United States.

Corresponding author: tahatton@mit.edu

Section S1. Materials

Pyrrole, chloroform, methanol, conductive multi-walled carbon nanotubes (diameter: 6 – 9 nm, purity: 95%), sodium perchlorate, tetrabutylammonium perchlorate, and sudan orange G, 2,4-dichlorophenol, 2-naphthol, 1-naphthylamine, bisphenol A, bisphenol S, metolachlor, ethinyl estradiol, propranolol hydrochloride, methyl orange, and rhodamine B were purchased from Sigma Aldrich, and were used as received throughout the study, without further purification or chemical modification unless otherwise noted. Polyvinylferrocene with a molecular weight of 50,000 g/mol was obtained from Polysciences and used as received. A platinum wire auxiliary electrode and an Ag/AgCl (3 M NaCl) reference electrode were purchased from BASi and stored as instructed. Flexible carbon cloths were obtained from FuelCellStore and used as received without pretreatment prior to electrochemical functionalization by electroactive polymers.

Section S2. Instrumentation

Scanning electron microscopic measurements were carried out using JEOL-6010LA SEM for general imaging and JEOL-6700 for high-resolution imaging. Samples for SEM were sputter-coated with a layer of gold/palladium (~10 nm) using a Desk II cold sputter/etch unit. Transmission electron microscopic measurements and energy dispersive X-ray spectroscopic elemental analysis were performed using JEOL 2010 Advanced High Performance TEM. The surface area measurements were carried out using Micromeritics ASAP2020 to determine nitrogen adsorption/desorption isotherm (ASAP2020, Micromeritics) followed by data fitting using the Brunauer–Emmett–Teller (BET) method. Samples for BET analysis were free-standing polymer films peeled off stainless-steel electrodes. Thermogravimetric analysis experiments were carried out using a TA Q50 instrument. Absorption spectra were collected using a Varian Cary 6000i UV-Vis spectrometer. Fluorescence spectroscopic measurements were performed using a Horiba Jobin Yvon spectrofluorometer. All electrochemical experiments were performed using a VersaSTAT4 potentiostat (Princeton Applied Research) with a three electrode configuration using an Ag/AgCl (3 M NaCl) electrode (BASi) and a platinum wire as the reference electrode and the counter electrode, respectively. All potential values reported in this work are referenced to the Ag/AgCl electrode. Ultraviolet photoemission spectra (UPS) were obtained using Physical Electronics PHI 5000 VersaProbe with a He(I) emission lamp (21.20 eV photon energy).

Section S3. Fabrication of ETAS Adsorbents.

Two types of ETAS adsorbents, carbon cloth (CC)-supported PVF/PPY and PVF/PPY/CNT, were prepared from electrochemical deposition under different conditions. The CC-supported PVF/PPY was prepared by simultaneous electro-polymerization of pyrrole and electro-precipitation of PVF using a precursor solution that contained 2 mg/mL PVF, 200 mM pyrrole, and 0.1 M tetrabutylammonia perchlorate in $CHCl_3$. Such a co-precipitation process occurred due to the strong π stacking interactions between the aromatic monomer (i.e., pyrrole) and the cyclopentadiene ring of ferrocene moieties in PVF,[1] generating a nanoporous electro-active binary polymeric surface suitable for ETAS applications. The deposition was performed by chronoamperometry at a potential of 0.7 V versus Ag/AgCl for a specified period of time (usually 10 min). To prepare the CC-supported PVF/PPY/CNT, 0.1 mg/mL metallic carbon nanotubes was added into the precursor solution followed by sonication for 2 h prior to electrochemical deposition. The CNT surface consisting of sp^2-carbon atoms exhibited non-covalent interactions with PVF and pyrrole, leading to a stable suspension with well-dispersed CNTs after the sonication treatment. The electrochemical deposition was carried out at a potential of 0.7 V versus Ag/AgCl for a specified period of time (usually 15 min). Two control samples, CC-supported PVF and CC-supported PPY, were also prepared to compare the adsorption capabilities for organic pollutants. CC-supported PVF was prepared by applying a potential of 0.7 V for 10 min versus Ag/AgCl in a chloroform solution containing 2 mg/ml PVF and 0.1 M tetrabutylammonium perchlorate. The CC-supported PPY was prepared by electrochemical polymerization of pyrrole at a potential of

0.6 V versus Ag/AgCl for 10 min in an aqueous solution containing 200 mM pyrrole and 0.1 M sodium perchlorate.

We measured the pH values before and after applying a high potential of 0.6 V to either the PVF/PPY adsorbent or the PVF/PPY/CNT adsorbent, and found that the pH of the solution remained at a value of about 6.9. This observation is reasonable since in our ETAS operation, we applied a constant potential instead of a constant current. The redox processes that may lead to water oxidation or proton reduction (thus resulting in a change in pH) occur only during the very brief initial charging period (within a few seconds), while the adsorption/desorption process takes a much longer time (a few hours). In other modes of electrochemical separation (e.g., application of a constant current), the water oxidation or proton reduction process is taking place over the entire course of the process, and thus could cause a significant change in the pH of the solution, as observed by an earlier study from our group,[2] which also develops a highly effective electrode design strategy that can mitigate the pH change during constant-current operations.

Section S4. Redox Polymer Electrode (RPE) Simulation

The current responses of a redox-active thin film during potential sweeping processes depend on the thickness of the film, or more specifically, the distances of redox sites from the electrode surface. In order to quantitatively describe such a dependence, we used a modified redox polymer electrode (RPE) model according to previous works reported by Bard *et al*[3-5] to simulate the voltammetric responses of PVF/PPY hybrid films with varying thicknesses. The details of the RPE simulations were reported in our previous work.[6] Briefly, the RPE model assumes that i) at the interface between the electrode surface and the redox-active film, the electron exchange process involves only the redox moieties near the electrode, and is described by the Butler-Volmer kinetics, and ii) charge transport in the bulk film is described by diffusion kinetics.[7] Such a model has been used for redox polymer films,[7,8] and also specifically for PVF films.[9] The redox polymer film is divided into a number of layers with an equal concentration of redox sites contained in each layer, and instantaneous amperometric responses were simulated when the potential of the electrode was linearly scanned. The experimentally observable parameters in our study were the peak currents at different scan rates during cyclic voltammetric scans. Slopes obtained from linear fits of the log(peak current) – log(scan rate) data contained information about the thicknesses of the PVF/PPY hybrid films on the carbon cloth substrate or the carbon nanotube scaffold. From the RPE simulations, we obtained relations between the slope and the thickness of the ferrocene-containing film. The parameters used include: the standard heterogeneous electron transfer rate constant of ferrocene (k^0 = 96 s^{-1} for PVF/PPY on CC derived from direct measurements of ferrocene monolayers self-assembled on gold[10] and the difference in the density of electronic states between carbon fiber and gold,[11] and 518 s^{-1} for PVF/PPY on the carbon nanotube due to enhanced electron transfer kinetics calculated using Gerisher-Marcus theory, see Section S4), transfer coefficient (α) for the Butler-Volmer kinetic equation (a value of 0.5 is usually assumed for ferrocene),[9] charge transport diffusion coefficient for PVF films with ClO_4^{-1} as the anion (D_{ct} = 1.06 × 10^{-9} cm^2/s)[9], formal potential of ferrocene (E^0 = 0.39 V for PVF/PPY on CC, and E^0 = 0.29 V for PVF/PPY on CNT, determined from CV measurements), the thickness for each layer in the RPE model (2 nm),[6] Faraday constant (F = 96485.3 C/mol), and the ideal gas constant (R =8.314 J/mol K). Understanding the charge transport processes using the RPE simulations sheds light on the multi-layer nature of a redox-active polymer film, as well as permits a better design and construction of RPEs for several applications in addition to ETAS, such as electrical energy storage,[12] molecular sensing,[13] and electrochemically controlled catalysis.[6]

Section S5. Gerischer-Marcus Calculations

Gerischer-Marcus (GM) theory describes the heterogeneous electron transfer kinetics using a formulism that considers the energy distribution of a redox species and the density of states in the electron phase, based on the following equation:

$$k_{ET} = \xi \int_{-\infty}^{\infty} \theta(E) f(E) \rho_F(E) W_{ox}(\lambda, E) dE$$

$$W_{ox}(\lambda, E) = \frac{1}{\sqrt{4\pi k_B T \lambda}} \exp\left(-\frac{\left(E - E_{F,redox} - \lambda\right)^2}{4 k_B T \lambda} \right)$$

where k_{ET} is the electron transfer rate constant at a given overpotential, ξ is the prefactor that appear in the GM formalism, $\theta(E)$ is the proportionality function, $\rho_F(E)$ is the density of states in the valence band of the electrode near the Fermi level, $f(E)$ is the standard Fermi-Dirac distribution function, $W_{ox}(\lambda, E)$ is a Gaussian function that depicts the energy-level distribution of the unoccupied states of the ferrocene/ferrocenium couple, k_B is the Boltzmann constant, $E_{F,redox}$ is the Fermi level of the ferrocene/ferrocenium couple, and λ is the solvent reorganization energy for ferrocene (a value of 0.5 eV was used in our calculation).[14] It is often assumed that $\theta(E)$ does not depend on the energy level, and ξ is independent of the underlying electrode material;[15,16] therefore, these two parameters cancel out when calculating the relative electron transfer rate constants. ϱ_F for CC and CNT was approximated by the intensities of the valence bands near E_F, measured by ultraviolet photoelectron spectroscopy (see main text Figure 4h). GM calculations were usually used to study the dependence of heterogeneous electron transfer kinetics of a redox species on the density of states of the electrode material.

Section S6. Simulations of Multi-Unit Stop-Flow Operations

Because the experimentally measured concentrations in the feed and receiving solutions were represented well by simulations of the equilibrium sorption processes with experimentally determined potential-dependent sorption isotherms used for the electrodes at each stage (see Main Text **Figure 3b and 3c**), we can, therefore, with confidence, use sorption isotherms obtained with the electrodes to predict the performance of other staged separation processes of interest. For practical applications at large scale, such separations are usually implemented in a continuous or semi-continuous mode with multiple physical separation units and direct contact between the feed and receiving phases. In our case, however, the transfer is mediated by the ETAS adsorbent, which cycles between the two streams, picking up solute from the feed solution and releasing it to the receiving solution. Simulations of these processes would allow an assessment to be made of the effects of parameters such as receiving-to-feed volume ratio, electrode mass per volume of feed, number of separation units (N_{unit}), etc., to optimize the overall design of a separation process for a given task. Moreover, we can now evaluate the potential benefits of exploiting counter-current operations, which are generally more effective than co-current systems. The systems simulated here are illustrated in **Figure S1** for a co-current multi-unit process, and in Main Text **Figure 5a** for a counter-current multi-unit process. Both processes are operated in a stop-flow fashion.

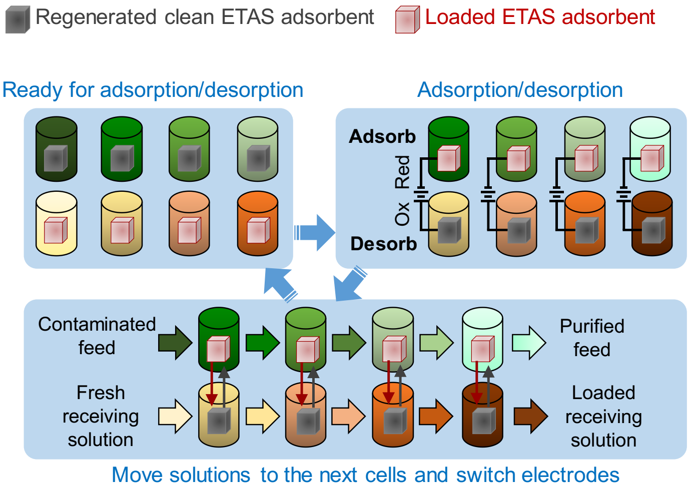

Figure S1. Illustration of the multi-unit stop-flow operation in a co-current fashion. A darker color of the solution in the cell indicate a higher pollutant concentration.

All cells are filled, and appropriate potentials are applied until equilibrium adsorption or desorption is reached. The solutions are then all transferred to the next cells – for instance, the feed solution from unit *n* is fed to the cell in unit *n*+1 and the receiving solution in unit *n* is fed to the cell in unit *n*+1 (for the counter-current operation, it is fed to unit *n*-1). At any given stage, the electrode that had been in equilibrium with the feed solution is transferred to the cell containing the new receiving solution, while the depleted electrode in the receiving solution cell is relocated to the feed solution cell. The electrodes are then activated again to drive the adsorption from the feed solution and desorption to the receiving solution at each unit. The material balances associated with each phase can be used to evaluate the equilibrium concentrations at each unit at the end of each cycle (**Figure S2**).

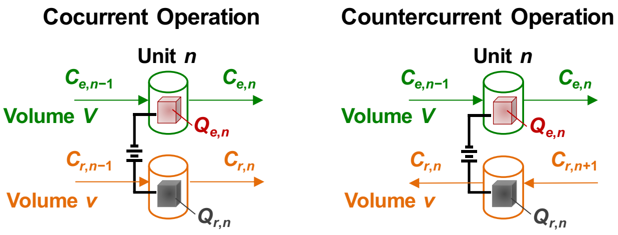

Figure S2. Schematics of the material balances at equilibrium at a given unit.

For the co-current case, volume V of the feed solution is fed to unit 1, with concentration C_{e0}, where it contacts electrode E_1 with loading Q_{r1}. This solution comes to equilibrium with the electrode, which now has loading Q_{e1}. The total mass of electrode is m. In the meantime, the electrode that was in contact with the feed volume in the previous cycle is now contacted with the stripping phase of volume v and initial concentration C_{r0}, and comes to equilibrium with the electrode, with loading Q_{r1}. In the next step, the feed solution that was in unit 1 is transferred to unit 2, where it contacts a second electrode E_2 that had been in equilibrium with the stripping solution with loading Q_{r2}. When the feed solution is equilibrated with the electrode, it is passed to unit 3, and the electrode is then exposed to the stripping solution with initial concentration C_{r1}. We can repeat this procedure for a given number of units, N_{unit}. To study the effects of important operating parameters, we express the material balances in terms of θ (= v/V) and ξ (= m/v). For any intermediate unit n, the material balances at equilibrium are:

$$C_{en} = C_{e,n-1} - \left(\frac{v}{V}\right)\left(\frac{m}{v}\right)(Q_{en} - Q_{rn})$$

$$= C_{e,n-1} - \theta\xi(Q_{en} - Q_{rn})$$

$$C_{rn} = C_{r,n-1} + \left(\frac{m}{v}\right)(Q_{en} - Q_{rn})$$

$$= C_{r,n-1} + \xi(Q_{en} - Q_{rn})$$

with $Q_{en} = Q_{en}(C_{en})$ and $Q_{rn} = Q_{rn}(C_{rn})$ given by the sorption isotherms determined experimentally under different potential conditions.

In the counter-current case, the feed stream equations are unchanged, but the stripping solution is such that the solution to unit n comes from unit n+1, rather than from unit n-1. Thus, for the nth unit we have:

$$C_{en} = C_{e,n-1} - \theta\xi(Q_{en} - Q_{rn})$$

$$C_{r,n+1} = C_{r,n} - \xi(Q_{en} - Q_{rn})$$

Here the equations must be solved iteratively. An initial guess for C_{r1} must be made, and then the equations solved for all stages. Convergence is achieved when the guessed C_{r1} leads to the prescribed concentration for the stripping solution added to unit N, which is generally 0.

The simulation results are shown in **Figure 5b, 5c and S3** for PVF/PPY adsorbents switching between 0.2 and 0.4 V, expressed in terms of the final concentrations in the feed and receiving phases normalized by the initial feed concentration (ψ, left axis), for different N_{unit}, θ and ξ values. The right axis of each panel shows the relative difference in concentration between the counter-current and co-current operations, defined as $(\psi_{ct} - \psi_{co})/\psi_{co} \times 100$, where ψ_{ct} and ψ_{co} are for counter-current and co-current operations, respectively.

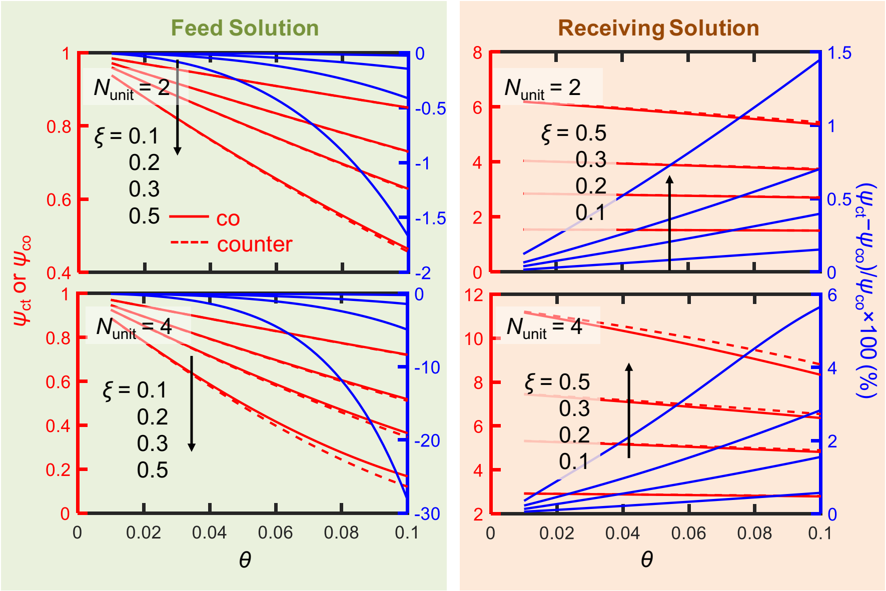

Figure S3. Simulated ψ values (left axis) with different N_{unit}, θ and ξ for the nonlinear sorption isotherm case. Right axis: relative difference in concentration between the counter-current and co-current operations, $(\psi_{ct} - \psi_{co})/\psi_{co} \times 100$.

As discussed in the Main Text, an unexpected finding was that there appears to be little difference in performance under co- and counter-current conditions; usually counter-current operations are much more favorable for multi-unit processes. This is a reflection of the shapes of the isotherms, in which the difference in loadings for the electrodes in the adsorption and desorption cells at any stage is almost independent of unit number; i.e., $Q_{en} - Q_{rn} = \Delta Q \approx$ constant. Under these conditions the mass balance equations reduce to

$$C_{en} = C_{e,n-1} - \theta \xi \Delta Q$$

$$C_{rn} = C_{r,n-1} + \xi \Delta Q$$

or, for counter-current operations,

$$C_{r,n+1} = C_{r,n} - \xi \Delta Q\,.$$

Thus, there is no effect of C_{rn} on C_{en}, and vice versa, so it is immaterial whether the system is in co-current or counter-current operation. The actual values of ΔQ are shown in **SI Figure S4**.

The conclusion above that there is little difference in co- and counter-current operations is not a general result and reflects the peculiarities of the isotherms for these specific electrodes. For other types of sorption isotherms, e.g., those following Henry's Law in which the adsorbed amount is directly proportional to the concentration in solution, ΔQ would be strongly concentration-dependent, and thus significant differences between the co-current and counter-current operations would be anticipated. To demonstrate this point, simulations were performed for an ETAS adsorbent having linear sorption isotherms Q_e (mg/g) = 100C_e (mg/L) and Q_r = 20C_e (mg/L) for the reduced and oxidized states, respectively, with the same set of N_{unit}, θ and ξ values used for generation of the curves in the nonlinear sorption case. It is evident that in the linear sorption isotherm case (**Figure 5d, 5e and S5**), the counter-current operation results in markedly improved separation effectiveness over the co-current case, with a lower final feed solution concentration and a higher final receiving solution concentration.

These simulations indicate that we can use experimentally determined, potential-dependent sorption isotherms to predict ETAS separation effectiveness under different operating conditions and device configurations. More importantly, for a given separation task with specified requirements such as feed or receiving phase concentration, number and geometry of operation units (related to capital cost) etc., the proposed simulation scheme based on multi-unit stop-flow operation mode could be used as a general framework for rational design and optimization of separation processes for large-scale operation.

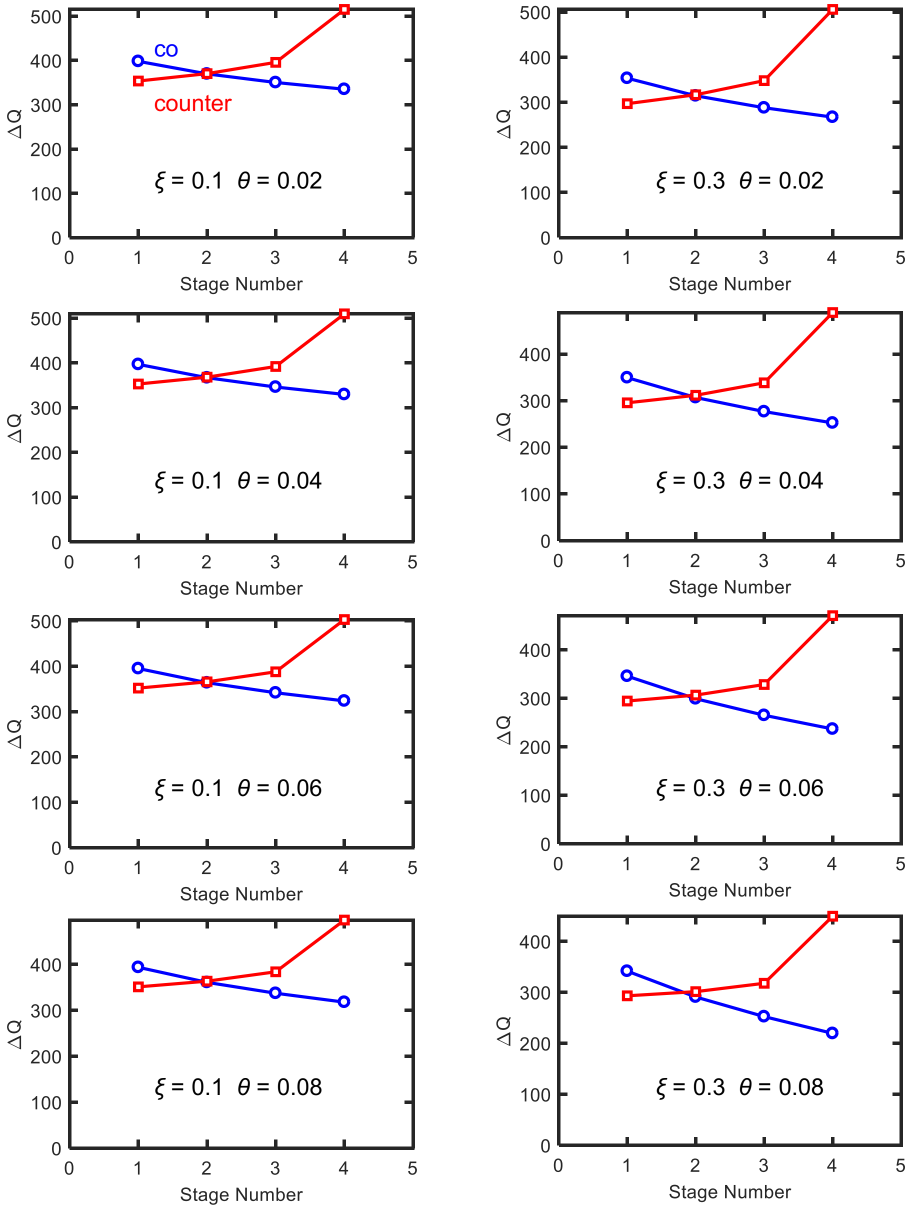

Figure S4. ΔQ versus stage number for a range of selected ξ and θ values (indicated in each panel), showing that ΔQ does not change significantly as a function of the stage number. Simulations were performed with the PVF/PPY ETAS adsorbent switching between 0.2 and 0.4 V.

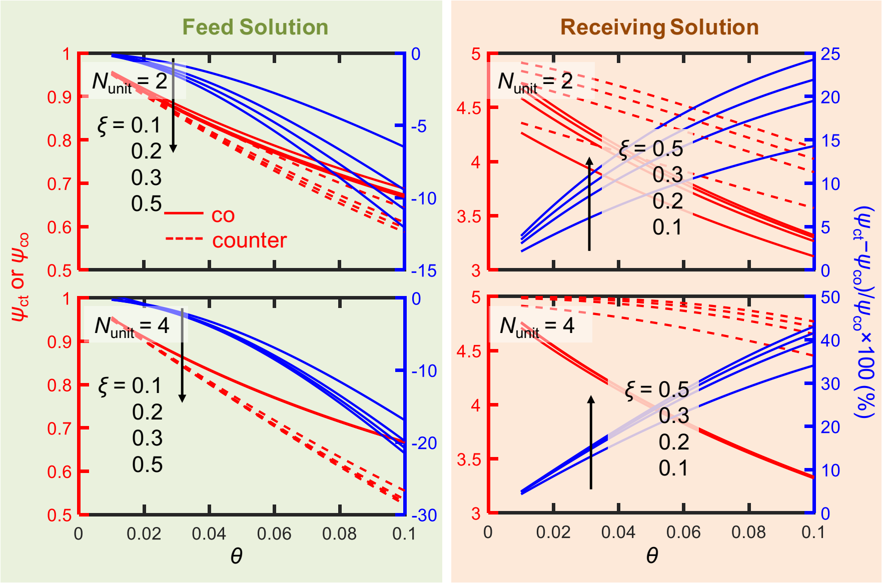

Figure S5. Simulated ψ values (left axis) with different N_{unit}, θ and ξ for the linear sorption isotherm case. Right axis: relative difference in concentration between the counter-current and co-current operations, $(\psi_{ct} - \psi_{co})/\psi_{co} \times 100$.

Section S7. Comparison with Alternative Separation Technologies

We provide a detailed figure-of-merit comparison between ETAS and the competing separation technology that targets uncharged organics, which is the conventional temperature swing adsorption/desorption methods. Other separation technologies such as distillation and liquid-liquid extraction are not suitable for the recovery/removal of these uncharged organic compounds. The volatilities of these organics are too low for distillation processes to work, and the possible counter-contamination of feed streams with organic solvents makes it unsuitable to employ liquid-liquid extraction to separate these organics. The state-of-the-art adsorbent materials used in conventional adsorption processes for removing organic pollutants are carbon nanomaterials, such as activated carbon (AC), carbon nanotubes (CNTs), and graphene-based materials; a handful of studies also reported the use porous metal oxides as adsorbent materials.[17, 18]

The economics and sustainability of a separation technology should be assessed in the context of an entire chemical process; important factors that need to be considered should include the fabrication and replacement costs of key components (e.g., sorbent materials, membrane modules), the capital cost of the equipment, and the energy cost.[19]

Carbon materials (such as AC used in thermal-swing separation processes) and organic polymeric materials (such as electrochemically active polymers (EAPs) used in ETAS) are considered inexpensive materials with low manufacturing costs, compared to other materials such as metal oxides.[20-24] The industrial scale manufacturing of carbon materials such as AC and CNTs has long been realized, so the production cost of these materials at large scale should be considerably lower than that for the ETAS adsorbents, which are new material systems and their synthesis has only been demonstrated on a bench scale. The ability to scale-up the fabrication of the electrochemically nanostructured multicomponentpolymeric materials need to be explored. The replacement cost of sorbents materials is associated with their performance stability. The performance stability of carbon-based adsorbents after multiple thermal swing cycles should be compared to the performance stability of EAP-based adsorbents after multiple electrical swing cycles. The regeneration efficiency of carbon adsorbents depends highly on the regeneration conditions, and usually ranges from 70% to almost 100%[17,18] (i.e., after one thermal swing cycle, the adsorbent performance degrades to ~70% to 100% compared to its initial state). For example, for AC-based adsorbents, air activation at 633 K results in a regeneration efficiency of 68% and steam activation at 1123 K can achieve a regeneration efficiency of 94%.[25] Therefore, the optimized regeneration condition for spent carbon adsorbents would make them reusable for multiple cycles. However, during the regeneration process, it is common to have carbon loss of ~5% (mass percentage).[17,18] As a conservative estimation, assuming a regeneration efficiency of 100% and carbon loss of 5%, the performance of carbon adsorbents would decrease by 50% after 13 cycles. On the other hand, the performance stability of EAP-based adsorbents after multiple electrical swings can be faithfully estimated by investigating the relation between the charge capacity and the number of electrical swing cycles. Over the course of multiple electrical swing cycles (i.e., repeated charging/discharging cycles), several factors might affect the performance stability of EAPs, including structural pulverization, shrinkage of polymer backbones, and polymer leaching from conductive substrates.[7,20,26,27] A good stability of the charge capacity indicates the structural integrity of the EAP system. For the PVF/PPY system studied here, electrical swing between 0.0 and 0.8 V versus Ag/AgCl for 300 cycles resulted in only ~1% charge capacity loss, indicating good stability of our ETAS adsorbent when subjected to repeated electric swing cycles. For further enhancement of the performance stability of ETAS adsorbents, several previously developed methods such hydrothermal treatment[1] or organic vapor deposition[28] could be employed.

The capital cost for separation equipment is usually significant; commonly, 50–90 % of the capital of chemical plants is invested into separation units.[29] The adsorption step in both ETAS and thermal-swing adsorption/desorption processes is usually implemented at ambient temperature and pressure, and thus the capital cost of the adsorbers should be comparable between these two separation technologies. However, the thermal-swing separation technology requires high temperatures for the desorption/regeneration step (usually at 500 – 900 °C); such high temperature operation demands the employment of costly materials for the equipment such as stainless steel-based alloys, and therefore considerably raises the capital cost of the desorber and its associated pipe networks.[25,30] In contrast, the regeneration/desorption step in ETAS is carried out under ambient conditions, therefore presumably requiring significantly less capital investment for the equipment. Additionally, ETAS shares common features with other electrochemical separation technologies such as capacitive deionization, and the often-cited advantages of electrochemical equipment include modularity and low cost.[2, 31] While the operation with multiple separation units also increases the capital cost,[32] ETAS can be implemented in a multi-stage cyclic fashion (as demonstrated in main text Figure 3) using a single separation unit to achieve a specified separation degree. Conventional thermal-swing adsorption can be also implemented in a single unit with alternating heating and cooling steps. However, for both separation technologies, effective operation usually requires a number of coupled separation units. Therefore, ETAS and conventional adsorption are comparable in terms of the capital cost associated with the number of separation units.

The primary factor that governs the difference in the economic viability between ETAS and the conventional thermal swing separation technology should be the energy cost. In ETAS, the energy cost comes from the electrical swing over the course of ETAS operation whereas in the conventional thermal swing adsorption/desorption process, the primary energy consumption stems from the thermal regeneration of spent adsorbent materials. We compare the energy consumption quantitatively between ETAS and the thermal swing separation technology based on the scheme illustrated in **Figure S6**.

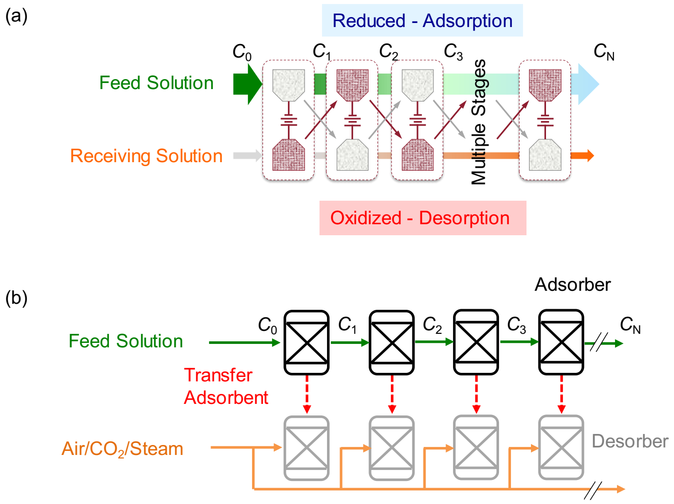

Figure S6. Illustration of the schemes used to quantify the energy consumption as a function of separation degree for ETAS (a) and the thermal swing adsorption/desorption process.

For ETAS operation, by numerically solving the coupled experimentally determined isotherms at the paired oxidation-reduction potentials, we can obtain the pollutant concentration after the *N*th stage (C_N), while in the meantime, we can quantify the electrical energy consumed using Eq. 3 in the main text. In ETAS, both adsorption and desorption occur at ambient temperature, so the only energy consumption is from the electricity used for the electrical swing. In the thermal swing separation process, adsorption occurs at ambient temperature while desorption (i.e., the regeneration of spent adsorbents) occurs at high temperature. The pollutant concentration after the *N*th adsorption unit can be calculated as the following. If we use fresh adsorbents in each adsorber, we will have the following relationship between C_N and C_{N-1} using the mass balance of the pollutant during adsorption:

$$\left(C_{N-1}-C_N\right)\frac{V_W}{m_{adsorbent,N}}=f_{isotherm}\left(C_N\right) \text{ (S1)}$$

where V_W is the volume of water in the feed, $m_{adsorbent,N}$ is the mass of the adsorbent in the *N*th adsorber, $f_{isotherm}\left(x\right)$ is the adsorption isotherm function, which can assume a variety of forms. For example, for a Langmuir isotherm,

$$f_{isotherm}(x) = \frac{K_L x}{1 + a_L x}$$

where K_L and a_L are the Langmuir constants; for a Freundlich isotherm,

$$f_{isotherm}(x) = K_F x^{b_F}$$

where K_F and b_F are the Freundlich constants.

Here we need to use Equation S1 to solve for C_N given the value of C_{N-1}. Equation S1 is generally nonlinear, and therefore we cannot solve for C_N analytically. We can numerically solve for C_N if we know C_{N-1}. Experimentally C_0 is known, and then we can iteratively solve for C_1, C_2, C_3, ……, C_N.

Depending on the specific condition for the regeneration step, the thermal energy consumption for activation of a unit mass of adsorbent is estimated as $m_a C_a \Delta T$, where m_a is the mass of the regeneration agent (e.g., air, CO_2 or steam), C_a is the heap capacity of the regeneration agent, and ΔT is the increase in temperature needed to reach the required temperature in the desorber.[17, 18, 25, 33]

Therefore, for ETAS, we can obtain a relation between the electrical energy consumed and the separation degree (C_1 − C_N)/ C_N × 100; for the conventional thermal swing separation process, we can also obtain a similar relation between the thermal energy consumed and the separation degree, given the information about the adsorption isotherm of the adsorbent materials.

The characteristics of an adsorption isotherm are dependent on the physio-chemical properties of the adsorbent material and the nature of the target organic pollutants to be separated. To estimate the energy consumption for the thermal swing separation process, we conducted a literature survey on several recently reported carbon materials (such as AC, CNTs, and graphene-based materials) used for water treatment by adsorption for removing various types of organics,[34-63] and used the reported adsorption isotherm data to calculate the energy consumption.

One important metric for assessing the energetic efficiency and the overall effectiveness of a separation technology is the energy consumption per unit mass of organics removed (J/g).[19] Based on the calculation scheme described above (see Figure S6), we quantified the energy consumption per unit mass of organics removed for ETAS operating with different potential pairs (**Figure S7**), as well as for the thermal swing adsorption/desorption process using the adsorption isotherms reported previously (**Figure S8, S9**).[34-63]

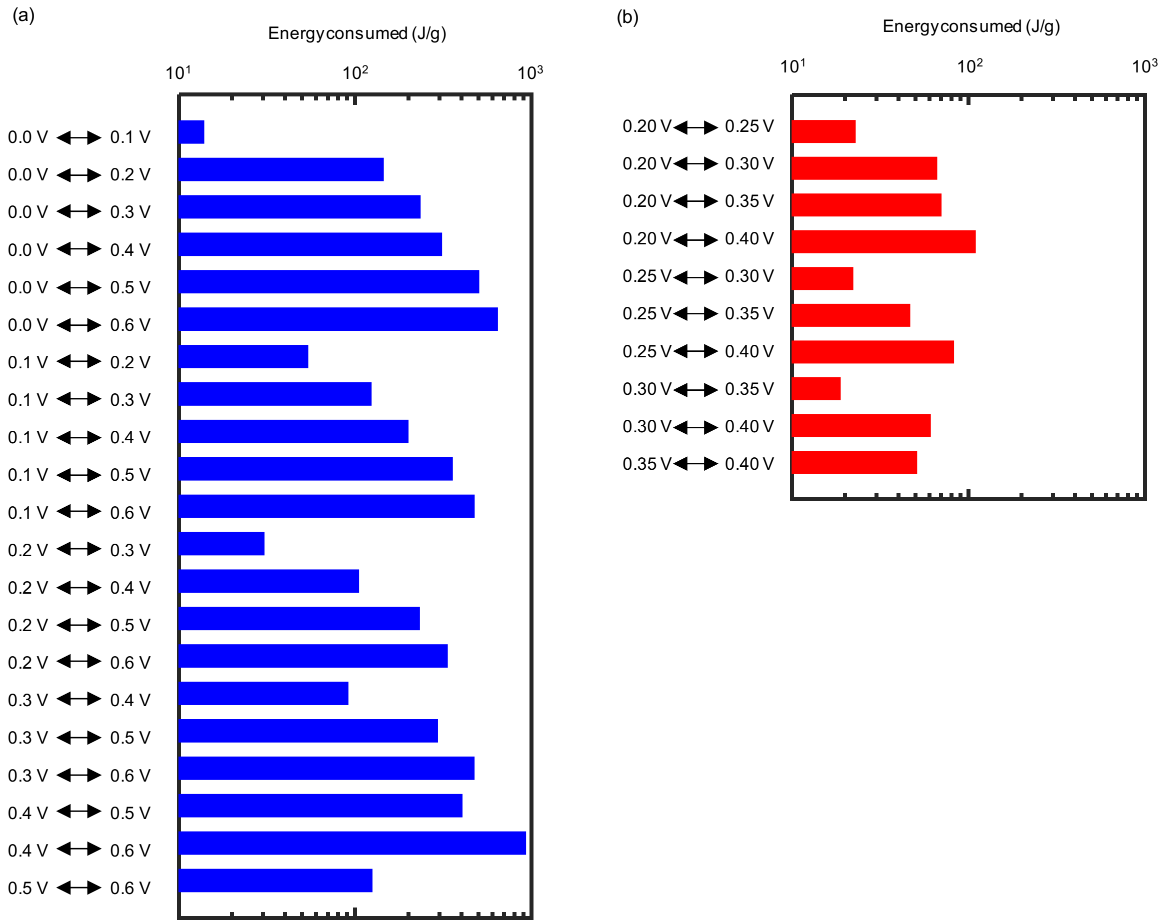

Figure S7. Calculated energy consumption per gram of SOG removed (J/g) for the ETAS multi-stage cyclic operation with different potential pairs using PVF/PPY as the ETAS adsorbent (a) and PVF/PPY/CNT as the ETAS adsorbent (b).

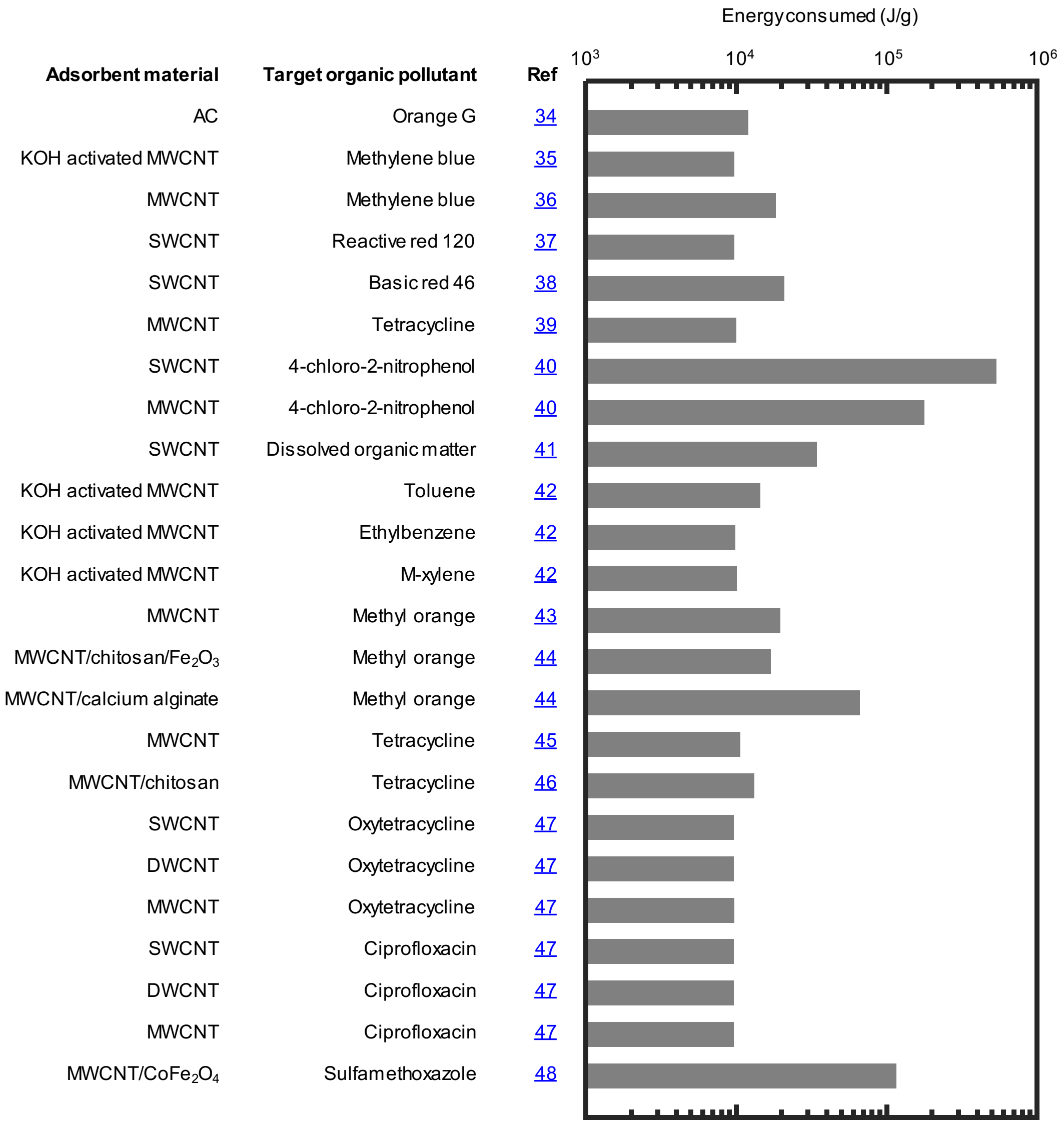

Figure S8. Calculated energy consumption per gram of organic removed (J/g) for the thermal swing adsorption/desorption process using carbon materials as the adsorbent. AC: activated carbon. SWCNT: single-walled carbon nanotube. DWCNT: double-walled carbon nanotube. MWCNT: multi-walled carbon nanotube.

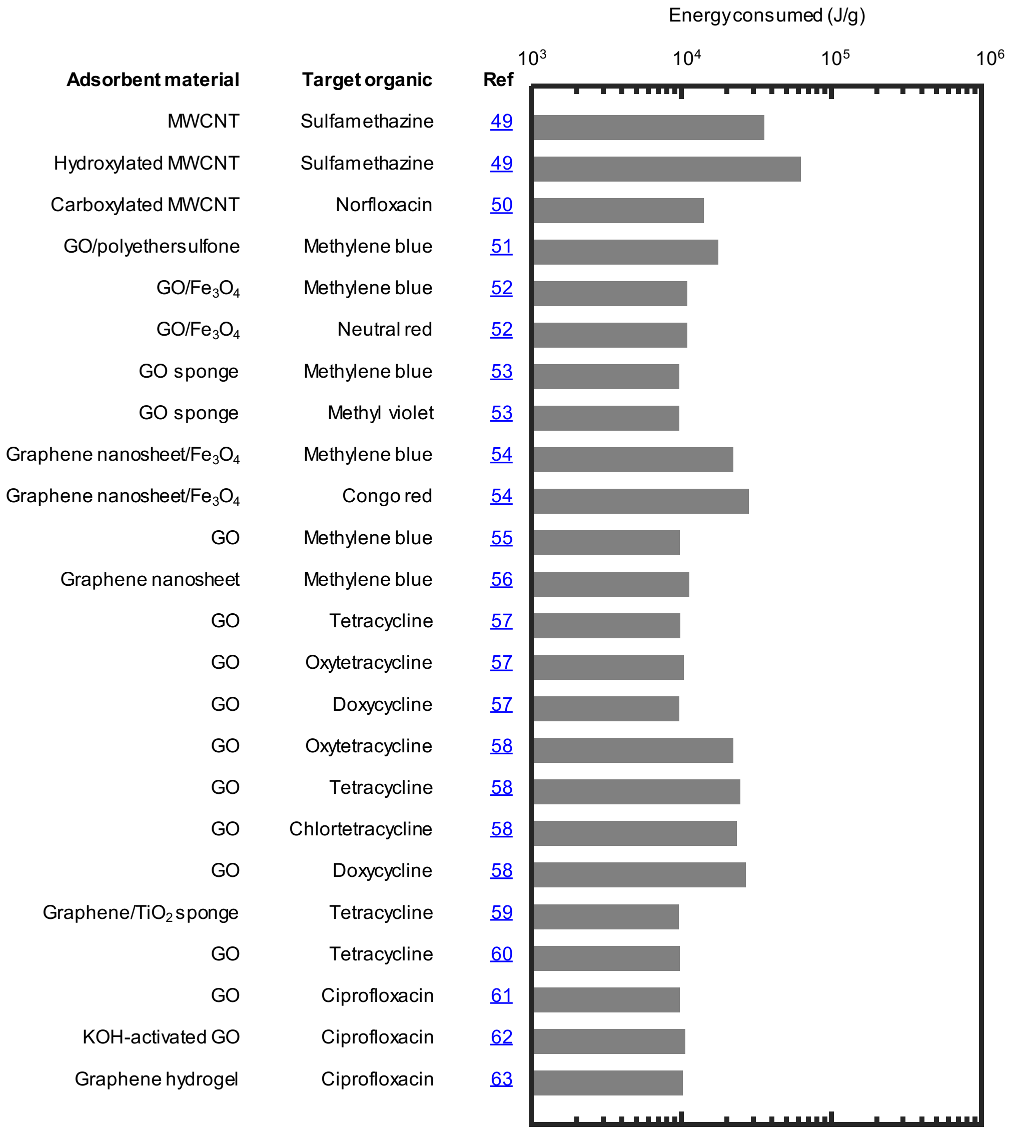

Figure S9. (Continued) Calculated energy consumption per gram of organic removed (J/g) for the thermal swing adsorption/desorption process using carbon materials as the adsorbent. AC: activated carbon. MWCNT: multi-walled carbon nanotube. GO: graphene oxide.

For ETAS operation, it is evident that a smaller difference between the paired potential results in a smaller energy use per gram of organics removed. Also, the use of PVF/PPY/CNT as the ETAS adsorbent is more energetically efficient than the use of PVF/PPY. More importantly, it is noteworthy that in general ETAS requires energy consumption around 10^2 to 10^3 J/g, whereas the thermal swing approach usually needs energy consumption around 10^4 J/g. Therefore, the energy efficiency in ETAS is improved significantly compared to that in the conventional thermal swing separation process. Our conclusion appears to be reasonable. It has been estimated that from a recent report that in US alternative technologies that do not rely on heat could make most separation processes 10 times more energy efficient.[19] To date, separation processes account for about 50% of US industrial energy use and about 15% of the nation's total energy consumption (commercial, transportation, residential, and industrial uses combined).[19] The majority of current separation processes involve the use of heat (such as conventional adsorption and distillation), and thus are energy intensive. These thermal separation methods combined account for 80 percent of the energy consumed for industrial separations, and therefore constitute the most attractive target for improvement. Therefore, it is reasonable to assume that the development of separation technologies that do not depend on heat (such as ETAS) would be critical for significant reduction of energy use in US. In fact, it has been estimated in 2015 by the US Department of Energy that new, energy efficient separation methods that do not heat, if applied to the US petroleum, chemical and paper manufacturing sectors alone, save 100 million tonnes of carbon dioxide emissions and 4 billion US dollars in energy costs per year.[64]

A more practical metric for comparing the economic viability between ETAS and the thermal swing separation technology should consider the cost of the energy source, which is electricity for ETAS and thermal energy for the thermal swing process. Based on the US Department of Energy and Energy Information Administration's national average data,[65] the cost of electricity and heat is about $30.5 and $ 13.4 per million BTU (British thermal unit, about 0.0003 kilowatt-hours), respectively.[19] Taking these costs into consideration, we calculated the cost required to remove one kilogram of organics (**Figure S10**), as a function of the typical range for the concentration of the organics. Considering the dependence of the energetic cost on the concentration range is important since it is necessary to compare separation technologies in a certain concentration range that is relevant to the target species to be separated. As shown in Figure S10, ETAS is more economically viable than the conventional thermal swing separation process.

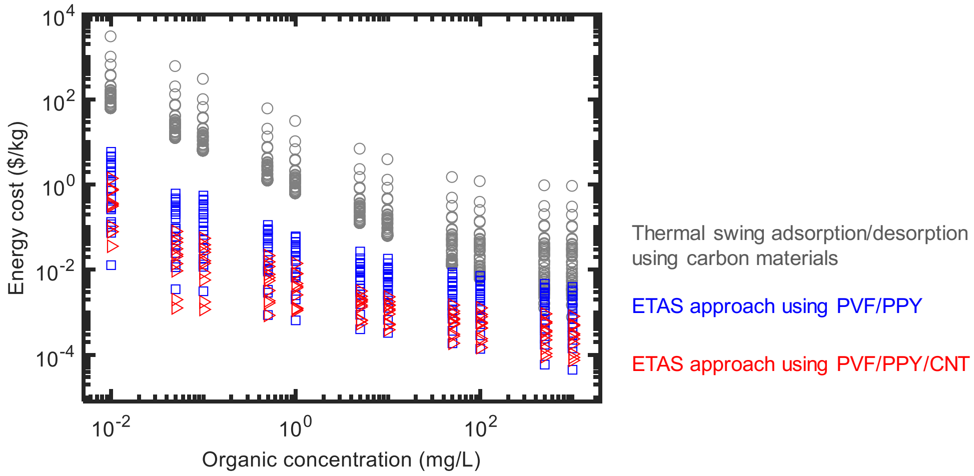

Figure S10. Comparison of the energy cost per kilogram of organics removed ($/kg) between the ETAS approach (blue squares: PVF/PPY as the ETAS adsorbent; red triangle: PVF/PPY/CNT as the ETAS adsorbent) and the conventional thermal swing adsorption/desorption process using carbon materials as the adsorbent (gray circles). For the ETAS approach, each symbol represents one potential pair used (see Figure S7) for separation of SOG. For the thermal swing approach, each symbol represents one combination of carbon-based adsorbent material and the target organic pollutant to be separated (see Figure S8, S9). The energy cost clearly depends on the specific adsorbent material used, the nature of the target organic to be separated, and the operation condition of the separation technology. This chart serves as an order-of-magnitude comparison of the energy cost between ETAS and the thermal swing separation process.

Furthermore, in a more realistic setting, the comparison of the economic viability between ETAS and the thermal swing process should also consider the following additional factors. Frist, the lifetime and the replacement costs of the adsorbent materials should be considered. Second, the adsorption/desorption kinetics should be factored in so as to estimate the organic removal rate or production rate (for value added organics). In general, the rate performance of the conventional thermal swing process has proved adequate for industrial scale operation, but the adsorption/desorption kinetics of ETAS has yet to be optimized. Moreover, the technology development of the ETAS processes should be performed to the scale at which deployment is required. The performance of ETAS will need to be evaluated at industrially operated test beds or multi-unit flow systems in order to investigate the scale-up ability of this technology. The thermal swing separation process has been well established and effectively demonstrated at an industrial scale.

The key metrics for evaluating the performance of ETAS and the thermal swing adsorption/desorption process are summarized in **Table S1**, and the important factors that need to be considered when comparing the two separation technologies are summarized in **Table S2**.

Table S1. Important metrics for assessing the performance of ETAS and the thermal swing separation technology.

Key metrics	**Units**
Organic adsorption capacity	mg g^{-1}
Average adsorption rate	mg g^{-1} min^{-1}
Energy consumption per unit mass organic removed	J g^{-1}
Energy cost (versus the organic concentration range)	\$ kg^{-1}

Table S2. Key factors to be considered when comparing ETAS and the conventional thermal swing separation technology.

	ETAS	**Thermal Swing Separation Technology**
Materials production cost	Low (EAPs)	Low (carbon materials)

Equipment capital cost	Adsorber: low Desorber: low	Adsorber: low Desorber: high
Energy cost	Low	High
Scale up cost	High	Low
Materials reusability	Moderate	Good
Equipment long term stability	Good	Moderate
Clean water production rate	Low	High

Section S8 Additional Supplementary Data

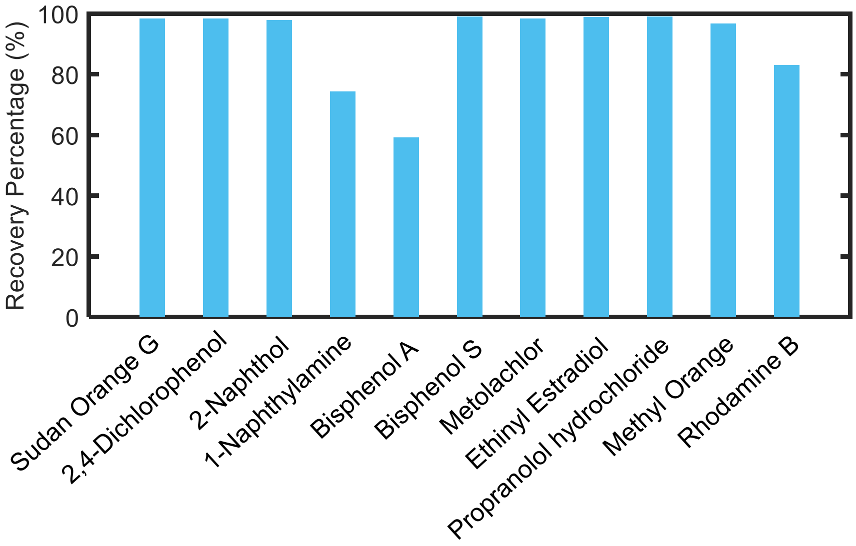

Figure S11. The recovery percentage (defined later) of organic pollutants tested in our study. Aqueous solutions of organic pollutants of known concentrations were put in contact with the PVF/PPY adsorbents for 18 to 26 hours while holding the potential at a constant value of 0.6 V, followed by desorption by methanol, ethanol or isopropanol. The recovery percentage was calculated using the quantity of organic found in both the aqueous phase and the organic phase divided by the initial known quantity. These results indicate that sudan orange G, 2,4-dichlorophenol, 2-naphthol, bisphenol S, metolachlor, ethinyl estradiol, propranolol hydrochloride, and methyl orange were not oxidatively degraded by application of a potential of 0.6 V under our experimental conditions, while 1-naphthylamine, bisphenol A, and rhodamine B showed oxidation degradation by 26%, 41%, and 17%, respectively. From previously reported studies, we found that the electrochemical potentials (converted to values versus Ag/AgCl) that may lead to oxidative decomposition of these organic pollutants in aqueous solutions were the following: 0.51 V for sudan orange G,[66] 0.82 V for 2,4-dichlorophenol,[67] 1.05 V for 2-naphthol,[68] 0.34 V for 1-naphthylamine,[69] 0.44 V for bisphenol A,[70] 0.75 V for bisphenol S,[71] advanced oxidation procedure needed for metolachlor,[72] 0.64 V for ethinyl estradiol,[73] 1.20 V for propranolol hydrochloride,[74] 1.21 V for methyl orange,[75] and 0.98 V for rhodamine B.[76]

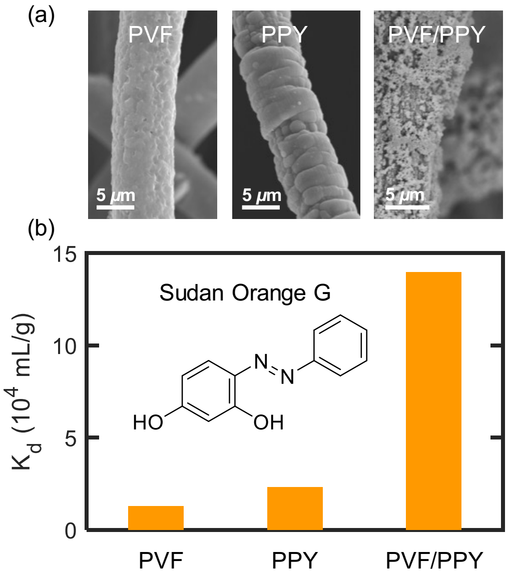

Figure S12. (a) SEM images of PVF/PPY, PVF, and PPY coated on carbon fibers. (b) K_d values of PVF, PPY and PVF/PPY.

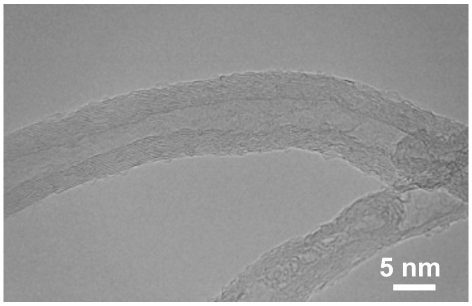

Figure S13. Representative high-resolution transmission electron microscopic (HRTEM) image of pristine multi-walled carbon nanotubes prior to modification by PVF/PPY, showing that the average diameter of the unmodified nanotubes is around 10 – 15 nm, and the average thickness of the nanotube wall was around 2 – 4 nm.

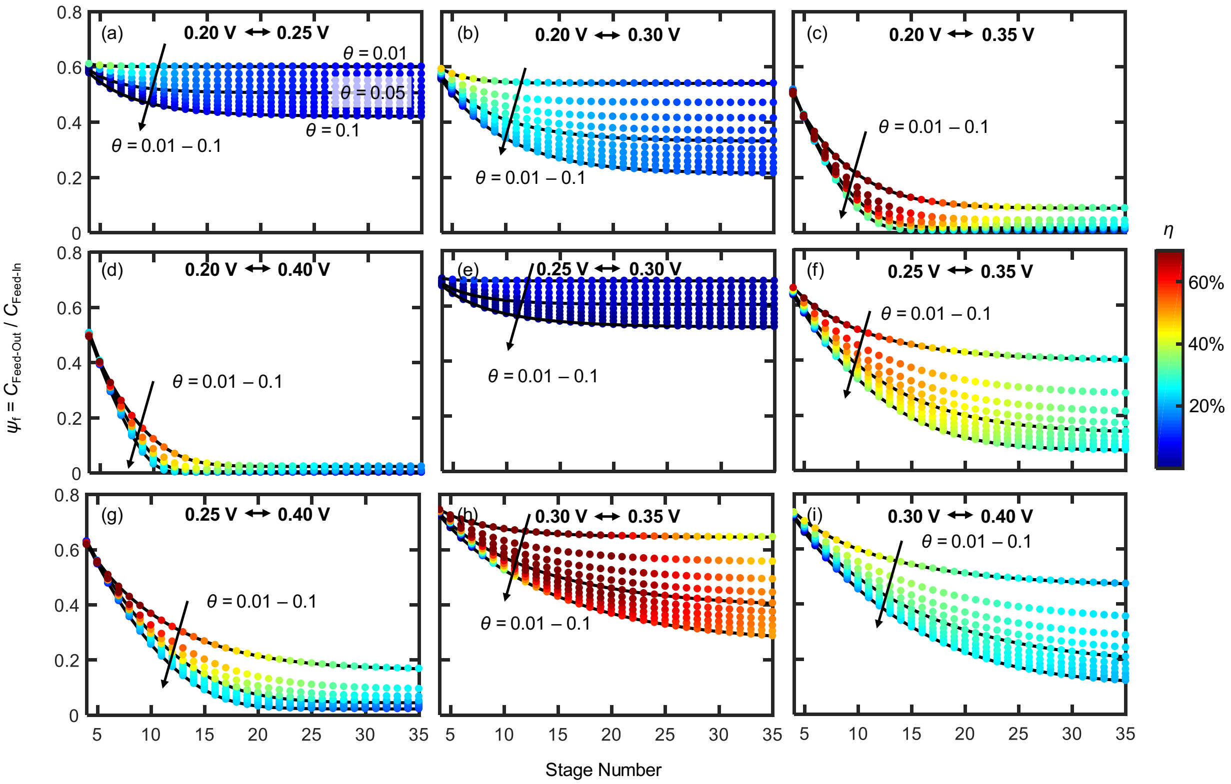

Figure S14. ψ_f-θ-η charts of PVF/PPY/CNT for the following potential pairs: (a) 0.20 V-0.25 V, (b) 0.20 V-0.30 V, (c) 0.20 V-0.35 V, (d) 0.20 V-0.40 V, (e) 0.25 V-0.30 V, (f) 0.25 V-0.35 V, (g) 0.25 V-0.40 V, (h) 0.30 V-0.35 V, and (i) 0.30 V-0.40 V.

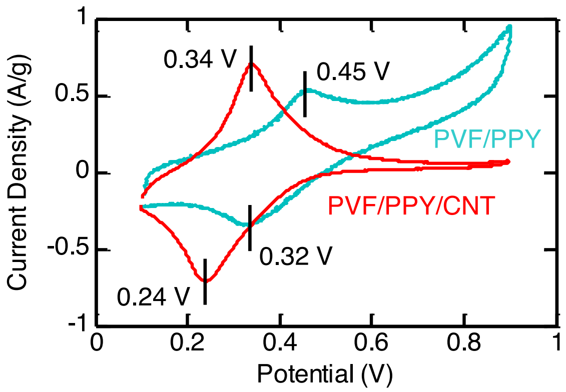

Figure S15. Representative cyclic voltammetric profiles of PVF/PPY and PVF/PPY/CNT obtained at 5 mV/s in 0.5 M $NaClO_4$ in a three-electrode configuration using Ag/AgCl as the reference electrode, showing that PVF/PPY/CNT had a lower ensemble-averaged formal potential of ferrocene than did PVF/PPY.

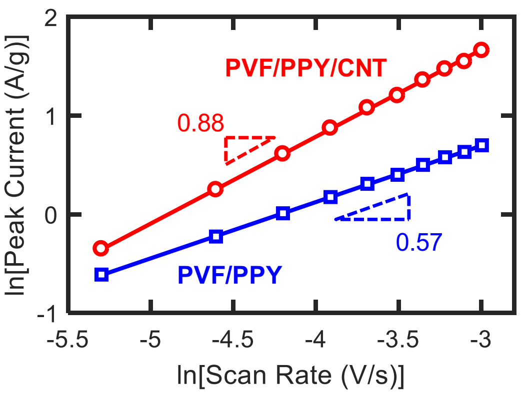

Figure S16. Logarithm of the CV peak current versus logarithm of the scan rate.

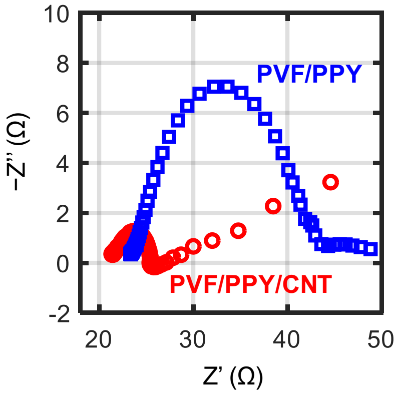

Figure S17. The electrochemical impedance spectra (EIS) for PVF/PPY (blue squares) and PVF/PPY/CNT (red circles) measured from 100 kHz to 10 mHz in an aqueous solution of 0.5 M $NaClO_4$, showing the difference between the two material systems in the interfacial charge-transfer resistance and the solution resistance, which are approximated by the diameter of the semicircle and the intercept on the Z' axis.

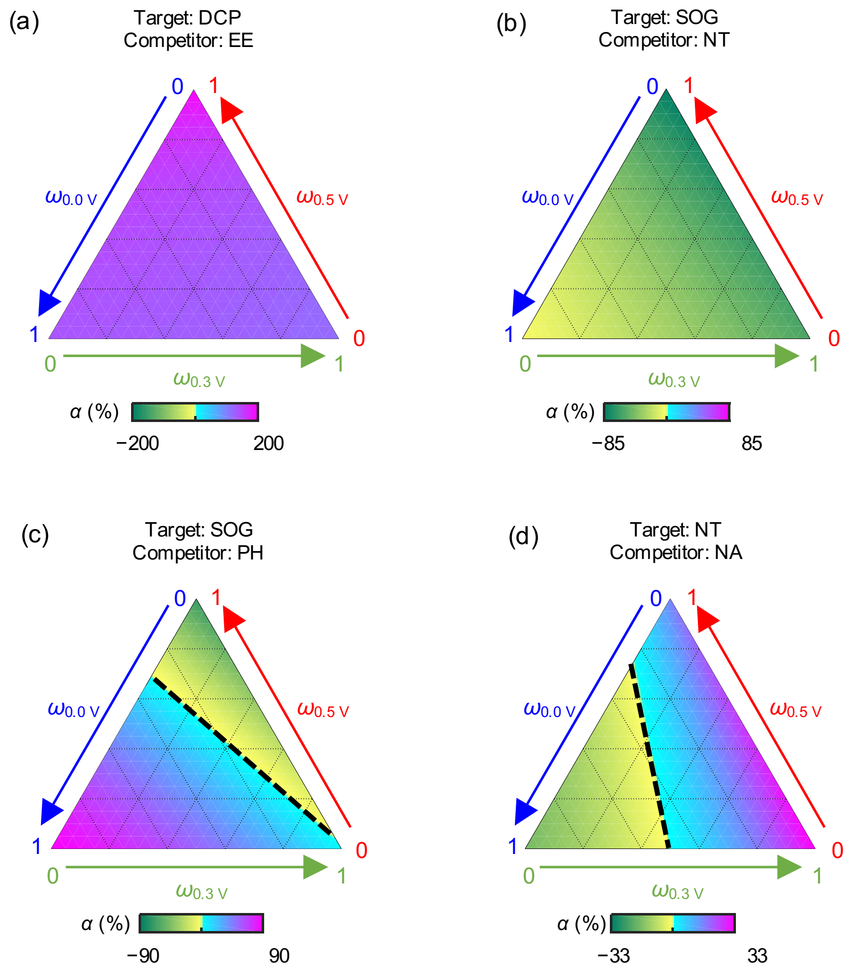

Figure S18. Selectivity factor (α) for a target organic in the presence of a competitor organic, defined as $\alpha\ (\%) = \frac{K_d^{target} - K_d^{competitor}}{K_d^{competitor}} \times 100$, as functions of the fraction of electrodes at 0.0, 0.3, and 0.5 V ($\omega_{0.0\ \mathrm{V}}$, $\omega_{0.3\ \mathrm{V}}$ and $\omega_{0.5\ \mathrm{V}}$). A negative α indicate the target species can be desorbed selectively and a positive α indicate the target species can be adsorbed selectively. Panels a – d show a few representative examples of selectivity maps (i.e., values as functions of $\omega_{0.0\ \mathrm{V}}$, $\omega_{0.3\ \mathrm{V}}$ and $\omega_{0.5\ \mathrm{V}}$), constructed in a way similar to the typical three-component phase diagram. DCP can only be desorbed selectively compared to EE (a), and SOG can only be selectively adsorbed compared to NT (b). Interestingly, in the presence of PH, SOG can be either selectively adsorbed or desorbed (c): selective adsorption or desorption of SOG is achieved with $\omega_{0.0\ \mathrm{V}} = 1$ or $\omega_{0.5\ \mathrm{V}} = 1$. The NT against NA case shows a different potential dependence than the SOG against PH (d): selective adsorption or desorption of NT is achieved with $\omega_{0.3\ \mathrm{V}} = 1$ or $\omega_{0.0\ \mathrm{V}} = 1$. The dashed line in (c) or (d) indicates that at these ($\omega_{0.0\ \mathrm{V}}$, $\omega_{0.3\ \mathrm{V}}$, $\omega_{0.5\ \mathrm{V}}$) combinations there is no selectivity between SOG and PH or between NT and NA. Such selectivity control is a unique and novel strategy because it is achieved through using electrically responsive materials, in which the external stimuli (potential or current) can be delivered to different electrodes locally and independently, without issues associated with mass diffusion or heat dissipation (often encountered when using chemical and thermal stimuli) that hamper such precise delivery over location.

Table S3. Values of physical parameters used in the calculations of energetic efficiencies.

Description	Value
Temperature (T)	298 K
ideal gas constant (R)	8.314 J/(K mol)
Faraday's constant (F)	96485 C/mol
density of water	1000 g/L
molecular weight of water	18 g/mol
molecular weight of SOG	214 g/mol
isotherm parameters (K_F, b_F) of the PVF/PPY system at the following potentials:	(K_F, b_F)
0 V	(231, 4.67)
0.1 V	(253, 5.07)
0.2 V	(247, 5.21)
0.3 V	(122, 3.80)
0.4 V	(40.7, 3.31)
0.5 V	(35.3, 3.59)
0.6 V	(31.2, 3.34)
the number of electrons transferred per unit mass of PVF/PPY during the anode-cathode switching with the following potential pairs:	
0.0 V / 0.6 V	1.61 mmol/g
0.2 V / 0.4 V	0.82 mmol/g
0.2 V / 0.3 V	0.23 mmol/g
isotherm parameters (K_F, b_F) of the PVF/PPY system at the following potentials:	(K_F, b_F)
0.2 V	(487, 6.72)
0.25 V	(357, 5.83)
0.3 V	(271, 5.32)
0.35 V	(152, 5.31)
0.4 V	(123, 5.43)
the number of electrons transferred per unit mass of PVF/PPY/CNT during the anode-cathode switching with the following potential pairs:	
0.2 V / 0.25 V	0.41 mmol/g
0.2 V / 0.3 V	0.73 mmol/g
0.2 V / 0.35 V	1.04 mmol/g

0.2 V / 0.4 V	1.40 mmol/g
0.25 V / 0.3 V	0.31 mmol/g
0.25 V / 0.35 V	0.64 mmol/g
0.25 V / 0.4 V	0.98 mmol/g
0.3 V / 0.35 V	0.34 mmol/g
0.3 V / 0.4 V	0.65 mmol/g

Section S9 References for the Supporting Information

1. W. D. Tian, X. W. Mao, P. Brown, G. C. Rutledge and T. A. Hatton, *Adv Funct Mater*, 2015, **25**, 4803-4813.
2. X. Su, K. J. Tan, J. Elbert, C. Ruttiger, M. Gallei, T. F. Jamison and T. A. Hatton, *Energ Environ Sci*, 2017, **10**, 1272-1283.
3. A. J. Bard and L. R. Faulkner, *Electrochemical methods : fundamentals and applications*, Wiley, New York, 2001.
4. P. J. Peerce and A. J. Bard, *J Electroanal Chem*, 1980, **114**, 89-115.
5. A. Merz and A. J. Bard, *J Am Chem Soc*, 1978, **100**, 3222-3223.
6. X. Mao, W. Tian, J. Wu, G. C. Rutledge and T. A. Hatton, *J Am Chem Soc*, 2015, **137**, 1348-1355.
7. G. Inzelt, *Conducting polymers : a new era in electrochemistry*, Springer, Heidelberg ; New York, 2012.
8. M. Peter, R. G. H. Lammertink, M. A. Hempenius and G. J. Vancso, *Langmuir*, 2005, **21**, 5115-5123.
9. T. B. Hunter, P. S. Tyler, W. H. Smyrl and H. S. White, *J Electrochem Soc*, 1987, **134**, 2198-2204.
10. J. F. Smalley, H. O. Finklea, C. E. D. Chidsey, M. R. Linford, S. E. Creager, J. P. Ferraris, K. Chalfant, T. Zawodzinsk, S. W. Feldberg and M. D. Newton, *J Am Chem Soc*, 2003, **125**, 2004-2013.
11. R. L. McCreery, *Chem Rev*, 2008, **108**, 2646-2687.
12. X. Mao, F. Simeon, D. S. Achilleos, G. C. Rutledge and T. A. Hatton, *J Mater Chem A*, 2013, **1**, 13120-13127.
13. L. S. Fan, Q. X. Zhang, K. K. Wang, F. H. Li and L. Niu, *Journal of Materials Chemistry*, 2012, **22**, 6165-6170.
14. G. A. Orlowski, S. Chowdhury and H. B. Kraatz, *Langmuir*, 2007, **23**, 12765-12770.
15. I. Heller, J. Kong, K. A. Williams, C. Dekker and S. G. Lemay, *J Am Chem Soc*, 2006, **128**, 7353-7359.
16. R. Sharma, J. H. Baik, C. J. Perera and M. S. Strano, *Nano Lett*, 2010, **10**, 398-405.
17. C. Santhosh, V. Velmurugan, G. Jacob, S. K. Jeong, A. N. Grace and A. Bhatnagar, *Chem Eng J*, 2016, **306**, 1116-1137.
18. V. K. Gupta, R. Kumar, A. Nayak, T. A. Saleh and M. A. Barakat, *Adv Colloid Interfac*, 2013, **193**, 24-34.
19. D. S. Sholl and R. P. Lively, *Nature*, 2016, **532**, 435-437.
20. Y. Shi, L. L. Peng, Y. Ding, Y. Zhao and G. H. Yu, *Chem Soc Rev*, 2015, **44**, 6684-6696.
21. G. P. Wang, L. Zhang and J. J. Zhang, *Chem Soc Rev*, 2012, **41**, 797-828.
22. J. Yan, Q. Wang, T. Wei and Z. J. Fan, *Adv Energy Mater*, 2014, **4**.
23. A. S. Arico, P. Bruce, B. Scrosati, J. M. Tarascon and W. Van Schalkwijk, *Nat Mater*, 2005, **4**, 366-377.
24. P. Simon and Y. Gogotsi, *Nat Mater*, 2008, **7**, 845-854.

25. S. Roman, B. Ledesma, A. Alvarez-Murillo and J. F. Gonzalez, *Fuel Process Technol*, 2013, **116**, 358-365.
26. T. Y. Liu, L. Finn, M. H. Yu, H. Y. Wang, T. Zhai, X. H. Lu, Y. X. Tong and Y. Li, *Nano Lett*, 2014, **14**, 2522-2527.
27. Y. Song, T. Y. Liu, X. X. Xu, D. Y. Feng, Y. Li and X. X. Liu, *Adv Funct Mater*, 2015, **25**, 4626-4632.
28. X. W. Mao, A. D. Liu, W. D. Tian, X. X. Wang, K. K. Gleason and T. A. Hatton, *Adv Funct Mater*, 2018, **28**.
29. J. G. Segovia-Hernandez, *Chem Eng Technol*, 2016, **39**, 2182-2182.
30. D. Ko and I. Moon, *Ind Eng Chem Res*, 2002, **41**, 93-104.
31. M. E. Suss, S. Porada, X. Sun, P. M. Biesheuvel, J. Yoon and V. Presser, *Energ Environ Sci*, 2015, **8**, 2296-2319.
32. M. Lozada-Hidalgo, S. Zhang, S. Hu, A. Esfandiar, I. V. Grigorieva and A. K. Geim, *Nat Commun*, 2017, **8**.
33. B. Ledesma, S. Roman, A. Alvarez-Murillo, E. Sabio and J. F. Gonzalez, *J Anal Appl Pyrol*, 2014, **106**, 112-117.
34. R. Gopinathan, A. Bhowal and C. Garlapati, *J Chem Eng Data*, 2017, **62**, 558-567.
35. J. Ma, F. Yu, L. Zhou, L. Jin, M. X. Yang, J. S. Luan, Y. H. Tang, H. B. Fan, Z. W. Yuan and J. H. Chen, *Acs Appl Mater Inter*, 2012, **4**, 5749-5760.
36. S. B. Wang, C. W. Ng, W. T. Wang, Q. Li and Z. P. Hao, *Chem Eng J*, 2012, **197**, 34-40.
37. E. Bazrafshan, F. K. Mostafapour, A. R. Hosseini, A. R. Khorshid and A. H. Mahvi, *J Chem-Ny*, 2013.
38. O. Moradi, *Fuller Nanotub Car N*, 2013, **21**, 286-301.
39. L. Zhang, X. Y. Song, X. Y. Liu, L. J. Yang, F. Pan and J. N. Lv, *Chem Eng J*, 2011, **178**, 26-33.
40. A. Mehrizad, M. Aghaie, P. Gharbani, S. Dastmalchi, M. Monajjemi and K. Zare, *Iran J Environ Healt*, 2012, **9**.
41. J. C. Lou, M. J. Jung, H. W. Yang, J. Y. Han and W. H. Huang, *J Environ Sci Heal A*, 2011, **46**, 1357-1365.
42. F. Yu, Y. Q. Wu, X. M. Li and J. Ma, *J Agr Food Chem*, 2012, **60**, 12245-12253.
43. D. L. Zhao, W. M. Zhang, C. L. Chen and X. K. Wang, *Procedia Environ Sci*, 2013, **18**, 890-895.
44. H. Y. Zhu, R. Jiang, L. Xiao and G. M. Zeng, *Bioresource Technol*, 2010, **101**, 5063-5069.
45. S. Alvarez-Torrellas, A. Rodriguez, G. Ovejero and J. Garcia, *Chem Eng J*, 2016, **283**, 936-947.
46. J. Ma, Y. A. Zhuang and F. Yu, *Phys Chem Chem Phys*, 2015, **17**, 15936-15944.
47. M. C. Ncibi and M. Sillanpaa, *J Hazard Mater*, 2015, **298**, 102-110.
48. F. Wang, W. L. Sun, W. Y. Pan and N. Xu, *Chem Eng J*, 2015, **274**, 17-29.
49. Q. Q. Yang, G. C. Chen, J. F. Zhang and H. L. Li, *Rsc Adv*, 2015, **5**, 25541-25549.
50. W. B. Yang, Y. P. Lu, F. F. Zheng, X. X. Xue, N. Li and D. M. Liu, *Chem Eng J*, 2012, **179**, 112-118.
51. X. Zhang, C. Cheng, J. Zhao, L. Ma, S. D. Sun and C. S. Zhao, *Chem Eng J*, 2013, **215**, 72-81.
52. G. Q. Xie, P. X. Xi, H. Y. Liu, F. J. Chen, L. Huang, Y. J. Shi, F. P. Hou, Z. Z. Zeng, C. W. Shao and J. Wang, *Journal of Materials Chemistry*, 2012, **22**, 25485-25485.
53. F. Liu, S. Chung, G. Oh and T. S. Seo, *Acs Appl Mater Inter*, 2012, **4**, 922-927.
54. Y. J. Yao, S. D. Miao, S. Z. Liu, L. P. Ma, H. Q. Sun and S. B. Wang, *Chem Eng J*, 2012, **184**, 326-332.
55. P. Bradder, S. K. Ling, S. B. Wang and S. M. Liu, *J Chem Eng Data*, 2011, **56**, 138-141.
56. T. H. Liu, Y. H. Li, Q. J. Du, J. K. Sun, Y. Q. Jiao, G. M. Yang, Z. H. Wang, Y. Z. Xia, W. Zhang, K. L. Wang, H. W. Zhu and D. H. Wu, *Colloid Surface B*, 2012, **90**, 197-203.
57. Y. Gao, Y. Li, L. Zhang, H. Huang, J. J. Hu, S. M. Shah and X. G. Su, *J Colloid Interface Sci*, 2012, **368**, 540-546.
58. Y. X. Lin, S. Xu and L. Jia, *Chem Eng J*, 2013, **225**, 679-685.

59. L. Q. Zhao, F. M. Xue, B. W. Yu, J. R. Xie, X. L. Zhang, R. H. Wu, R. J. Wang, Z. Y. Hu, S. T. Yang and J. B. Luo, *J Nanopart Res*, 2015, **17**.
60. E. E. Ghadim, F. Manouchehri, G. Soleimani, H. Hosseini, S. Kimiagar and S. Nafisi, *Plos One*, 2013, **8**.
61. H. Chen, B. Gao and H. Li, *J Hazard Mater*, 2015, **282**, 201-207.
62. F. Yu, J. Ma and D. S. Bi, *Environ Sci Pollut R*, 2015, **22**, 4715-4724.
63. J. Ma, M. X. Yang, F. Yu and J. Zheng, *Sci Rep-Uk*, 2015, **5**.
64. US Dept Energy Advanced Manufacturing Office. Bandwidth Study on Energy Use and Potential Energy Saving Opportunities in U.S. Petroleum Refining (US Dept Energy, 2015).
65. U.S. Energy Information Adminstration, Short-Term Energy Outlook Report 2018, https://www.eia.gov/
66. L. Pereira, A. V. Coelho, C. A. Viegas, M. M. C. dos Santos, M. P. Robalo and L. O. Martins, *J Biotechnol*, 2009, **139**, 68-77.
67. X. L. Zhu, K. X. Zhang, C. Z. Wang, J. N. A. Guan, X. Yuan and B. K. Li, *Sci Rep-Uk*, 2016, **6**.
68. M. Panizza and G. Cerisola, *Electrochim Acta*, 2003, **48**, 3491-3497.
69. E. Morsbach, M. Nesselberger, J. Warneke, P. Harz, M. Arenz, M. Baumer and S. Kunz, *New J Chem*, 2015, **39**, 2557-2564.
70. A. T. Wang, Y. L. Wei and C. Wang, *J Anal Chem+*, 2015, **70**, 67-71.
71. Z. X. Zheng, J. J. Liu, M. Wang, J. Q. Cao, L. Li, C. M. Wang and N. C. Feng, *J Electrochem Soc*, 2016, **163**, B192-B199.
72. M. A. Quiroz, E. R. Bandala and C. A. Martinez-Huitle, *Pesticides - Formulations, Effects, Fate*, 2011, 685-730.
73. C. Y. Li, *Bioelectrochemistry*, 2007, **70**, 263-268.
74. I. Baranowska and M. Koper, *J Brazil Chem Soc*, 2011, **22**, 1601-1609.
75. H. M. Yang, J. T. Liang, L. Zhang and Z. H. Liang, *Int J Electrochem Sc*, 2016, **11**, 1121-1134.
76. J. M. Austin, I. R. Harrison and T. I. Quickenden, *J Phys Chem-Us*, 1986, **90**, 1839-1843.